communications biology

A Nature Portfolio journal

Article

https://doi.org/10.1038/s42003-026-09807-4

Intracellular complement Factor H promotes tumor progression through modulation of cell cycle and actin cytoskeleton

Mikel Rezola Artero[1,2], Andrea Minery[1], Margot Revel[1], Angela Armento[3], Mohamed-Ali Jarboui[3,4], Idris Boudhabhay[1,5], Marina de Castro Deus[1], Alessandra Zarantonello[1], Emma Fleury[1], Lou Segarra[1], Alaeddine Redissi[1], Nicolas S. Merle[1,5], Marie-Agnes Dragon-Durey[1,5,6], Catherine Monnot[1], Catherine Sautes-Fridman[1], Jordan D. Dimitrov[7], Wolf Herman Fridman[1], Marius Ueffing[3,8] & Lubka T. Roumenina[1,5] ✉

Overexpression of complement genes in the tumor microenvironment, including Factor H (FH), is a strong predictor of poor prognosis in multiple cancers. Its canonical functions in the bloodborne complement cascade, though, cannot explain this prognostic impact. Here, we demonstrate that FH operates within the intracellular space in fibroblasts and tumor cells. By transcriptomics approach in patient tumors, cellular and biochemical assays we revealed that the prognostic impact of FH overexpression is mediated mainly by its cell-intrinsic functions in tumor-promoting fibroblasts and malignant cells. Intranuclear FH interacts with the cell cycle-transcription factor E2F3. FH also promotes proliferation by lowering the nuclear p53 pool. Moreover, in ccRCC cancer cells, FH also regulates cytoskeleton organization and cell morphology, potentially, via interaction with the actin capping CapZ complex. Therefore, complement FH acts as a multitasking effector, regulating cell cycle and actin polymerization, challenging the paradigm of extracellular space-restricted functioning, considered for many complement proteins.

The innate immune complement proteins have gained considerable interest in the recent years both as pathologic drivers and therapeutic targets in cancer[1–4]. The available complement therapeutics target the plasma complement cascade, aiming either to harness complement-mediated cytotoxicity, destroying tumor cells, or to curb the complement-mediated chronic inflammation[5–7]. Clinical trials revealed considerable patient response heterogeneity to different complement therapeutics, suggesting that even if the drug target is present, it may not be accessible to the drug and/or acting by a different mechanism[2].

Recent studies revealed that complement proteins are not restricted to plasma but can be overexpressed in the tumor[4] and act intracellularly[8,9]. The discovery of the intracellular complement opened a new gateway to explore previously unanticipated mechanisms impacting tumor growth. We revealed that the overexpression of the complement regulator Factor H (FH) correlates with poor prognosis in clear cell renal cell carcinoma (ccRCC, the most frequent type of renal cancer) and lung adenocarcinoma, but this impact was unrelated to the activation of the complement cascade or immune infiltration[10]. It was observed that the intracellular presence of FH

[1]Centre de Recherche des Cordeliers, Inflammation, Complement and Cancer team, Sorbonne Université, Inserm, Université Paris Cité, Paris, France. [2]Department of Bacteriology and Immunology, Haartman Institute, and Translational Immunology Research Program, University of Helsinki, Helsinki, Finland. [3]Department for Ophthalmology, Institute for Ophthalmic Research, Eberhard Karls University of Tübingen, Tübingen, Germany. [4]Core Facility for Medical Bioanalytics, Institute for Ophthalmic Research, Eberhard-Karls University of Tuebingen, Tübingen, Germany. [5]University Hospital Federation (FHU) COMET, Paris, France. [6]Laboratoire d'Immunologie, Hôpital Européen Georges Pompidou, APHP, Paris, France. [7]Centre de Recherche des Cordeliers, Inflammation, Immunopathology and therapeutic immuno-intervention, Sorbonne Université, Inserm, Université Paris Cité, Paris, France. [8]German Center for Neurodegenerative Diseases (DZNE), Tübingen, Germany. ✉e-mail: lubka.roumenina@inserm.fr

associated with enhanced proliferation, viability and migration of tumor cells by a still unknown mechanism[10]. Interestingly, other cell types in the tumor microenvironment also contain FH, especially fibroblasts[10] which have been associated to ccRCC progression[11].

FH is a promising therapeutic target in cancer[7,12,13]. The phase 1 clinical trial (NCT04314089) of the GT103 mAb targeting tumor surface-bound FH showed promise in refractory lung cancer[14]. Uncovering how FH acts in the tumor microenvironment and the contribution of cell-intrinsic/intracellular FH is critical to understand and potentially predict response to therapy across cancer types.

Here, we unravel the pro-tumoral mechanism of action of FH in ccRCC cancer cells and fibroblasts. We discovered that intracellular FH enables cancer hallmarks such as cell cycle progression and evasion of growth suppression by entering in the nucleus to interact with the Rb/E2F complex and control p53 activation. This mechanism could explain why *CFH* (encoding FH) overexpression is associated with poor clinical outcomes in different forms of cancer.

Results

CFH is overexpressed and correlates with poor prognosis in ccRCC

To evaluate the prognostic impact of *CFH* at the mRNA level, we investigated *CFH* expression in the TCGA ccRCC (KIRC) cohort. *CFH* expression was increased in tumors compared to normal adjacent tissue (Supplementary Fig. 1A) and was associated to higher tumor stage (Supplementary Fig. 1B) and grade (Supplementary Fig. 1C). Furthermore, elevated *CFH* also associated to shorter PFS (Fig. 1A) and Overall Survival (OS) (Supplementary Fig. 1D) even after adjustment for age, tumor grade, stage and sex (Supplementary Fig. 1E–H).

To identify the type of *CFH*-expressing cells within the tumor microenvironment, we interrogated a snRNA-seq dataset comprising 20 different ccRCC primary tumors [13]. *CFH* expression was detected in fibroblasts and cancer-associated fibroblasts "fibroblasts (CAF)", mural cells (pericytes and smooth muscle cells), endothelial cells and malignant cells (Fig. 1B, C). Among them, fibroblasts (CAF) presented the highest *CFH* expression levels (Fig. 1C). This was further confirmed with the analysis of spatial transcriptomics data from 24 ccRCC tumors [20], where we observed the high *CFH* expressing spots in both tumor core and stroma (Fig. 1D). Interestingly, over 80% of the tumors exhibited significant spatial co-localization between high MCP counter fibroblast scores and *CFH* expression (Supplementary Fig. 2). Immunofluorescence staining of primary ccRCC tumors (Fig. 1E) revealed FH co-localization with α-SMA positive fibroblasts (Fig. 1F) and CA9 positive cancer cells (Fig. 1G) in agreement with the transcriptomic data.

Comparisons between tumor and healthy adjacent tissue revealed that *CFH* was overexpressed in tumor cells relative to proximal tubular cells (the cells from which ccRCC originates) (Supplementary Fig. 3A, B), and in fibroblast (CAF) compared to kidney fibroblast (Supplementary Fig. 3C). Gene set enrichment analysis revealed that *CFH*-expressing cancer cells and fibroblasts were enriched for pro-inflammatory cytokine stimulation gene signatures (Supplementary Fig. 3D, E).

Local *CFH* expression in ccRCC is upregulated by pro-inflammatory cytokines

To explain the differences in *CFH* expression between tumor and healthy tissue, we explored cytokine-mediated regulation of local FH production. Consistent with prior GSEA results, correlation network analysis between *CFH* and various cytokines present in the tumor microenvironment revealed a strong positive correlation with the inflammatory cytokine: *IL6*, the pro-fibrotic cytokines: *TGFB1* and *TGFB3*, and various chemokines: *CCL26*, *CCL13*, *CCL11* and *CXCL5* (Supplementary Fig. 4A). Among these, *IL6* had a particularly high positive correlation with *CFH* (Supplementary Fig. 4B), which was also observed across different renal cell carcinoma cell lines (Supplementary Fig. 4C).

To further dissect this association, we employed the human ccRCC cell lines A498 and Caki-1. We attempted to isolate CAF from fresh ccRCC tumors unsuccessfully, consistent with the lack of established protocols or commercially available ccRCC CAF lines[15,16]. To overcome this hurdle and to account for the fact that *CFH* expression is a common phenomenon in fibroblasts from different origin[17], we employed the fibroblast cell line BJ, which expresses CAF markers such as α-SMA and FAP even in the absence of cancer-conditioned medium or TGF-β stimulation[18,19]. Quantigene *CFH* expression analysis of cells incubated for 24 h with either IL-1β, IL-6, TNF-α or TGF-β, revealed that IL-6 was the strongest inducer of *CFH* expression in ccRCC cell lines, whereas IL-1β and TNF-α induced *CFH* expression in BJ fibroblasts (Supplementary Fig. 4D–F). ELISA confirmed the increased production of FH by IL-6 stimulation in all the ccRCC cell lines (Supplementary Fig. 4G, H), and by IL-1β and TNF-α in BJ fibroblasts (Supplementary Fig. 4I). On the other hand, silencing *CFH* did not alter the cytokine secretion profile of the fibroblasts (Supplementary Fig. 4J–L).

Characterization and localization of intracellular FH in ccRCC cancer cells and fibroblasts

In ccRCC, the intracellular location of FH associates with tumor progression and cancer cell fitness[10]. Considering these findings, we aimed to dissect further the characteristics of intracellular FH in ccRCC cancer cells and in fibroblasts. Western Blot revealed that intracellular FH presented a lower molecular weight in comparison to its secreted form in the supernatant (SN) and plasma purified FH (Fig. 2A). The specificity of these bands in lysates and SN was confirmed by silencing experiments (Fig. 2B, C). In addition to the BJ cell line, we also evidenced the presence of an intracellular lower molecular weight band for FH in primary NHDF fibroblasts (Fig. 2B), emphasizing that this is a more general phenomenon.

To explore the intracellular localization of FH, subcellular fractionation was performed on both ccRCC cells and fibroblasts (Fig. 2D, E), and their purity was confirmed by the expected localization of control proteins (GAPDH, cytochrome c and histone 3). Most of the intracellular FH was present in the organelle fraction, consistent with the cytoplasmic cell staining (~60%+/-7) as previously reported[10]. Strikingly, we also observed the presence of intracellular FH in the nuclear and cytosolic fractions across cells (Fig. 2D, E). Partial co-localization of FH with the nuclei (~40%+/-7 of the signal) was observed by confocal microscopy on A498 ccRCC cells using polyclonal anti-FH (Fig. 2F) and confirmed by OX24, as well as on ccRCC tumor tissues stained by immunohistochemistry with OX24 (Fig. 2G) or by immunofluorescence with the rabbit polyclonal anti-FH (Fig. 2H). Moreover, we identified a putative nuclear localization signal (NLS) spanning the sequence between CCP1 and CCP2 (Complement Control Protein domains 1 and 2) of FH using the cNLS Mapper software[20] (Supplementary Fig. 5).

Intracellular FH interacts with proteins associated with the F-actin capping complex and the Rb/E2F pathway

To explore the functional significance of intracellular FH in ccRCC cells and fibroblasts, we performed FH co-immunoprecipitation (Ip) in cell lysates followed by mass-spectrometry to identify FH interacting partners (Supplementary Fig. 6A). Two monoclonal antibodies (mAb OX24 against an N-terminal epitope of FH (CCP5) and mAb C18/3 against a C-terminal epitope of FH (CCP20)) were employed after validation by Western Blot (Supplementary Fig. 6B, C). Ip with the C18/3 mAb co-immunoprecipitated 71 identified FH interacting candidates for A498 cells and 20 candidates for BJ fibroblasts (Supplementary Fig. 7A, B and Supplementary Table 3). Among these two sets, there were 10 common interacting candidates containing members from the Rb-E2F complex (Fig. 3A, B). Gene Ontology analysis of the BJ candidate set only identified interacting candidates related to the Rb-E2F complex (Fig. 3C), whereas analysis in the A498 set also identified proteins related to the actin cytoskeleton organization (Fig. 3D).

To validate our mass spectrometry results, we evaluated the interaction between FH and the common interacting candidates found in BJ and A498 cells (TJP1, E2F3, E2F4, TFDP1 and TFDP2) or unique to A498 cells (CAPZB and CREB1). In protein-protein interaction ELISAs at normal

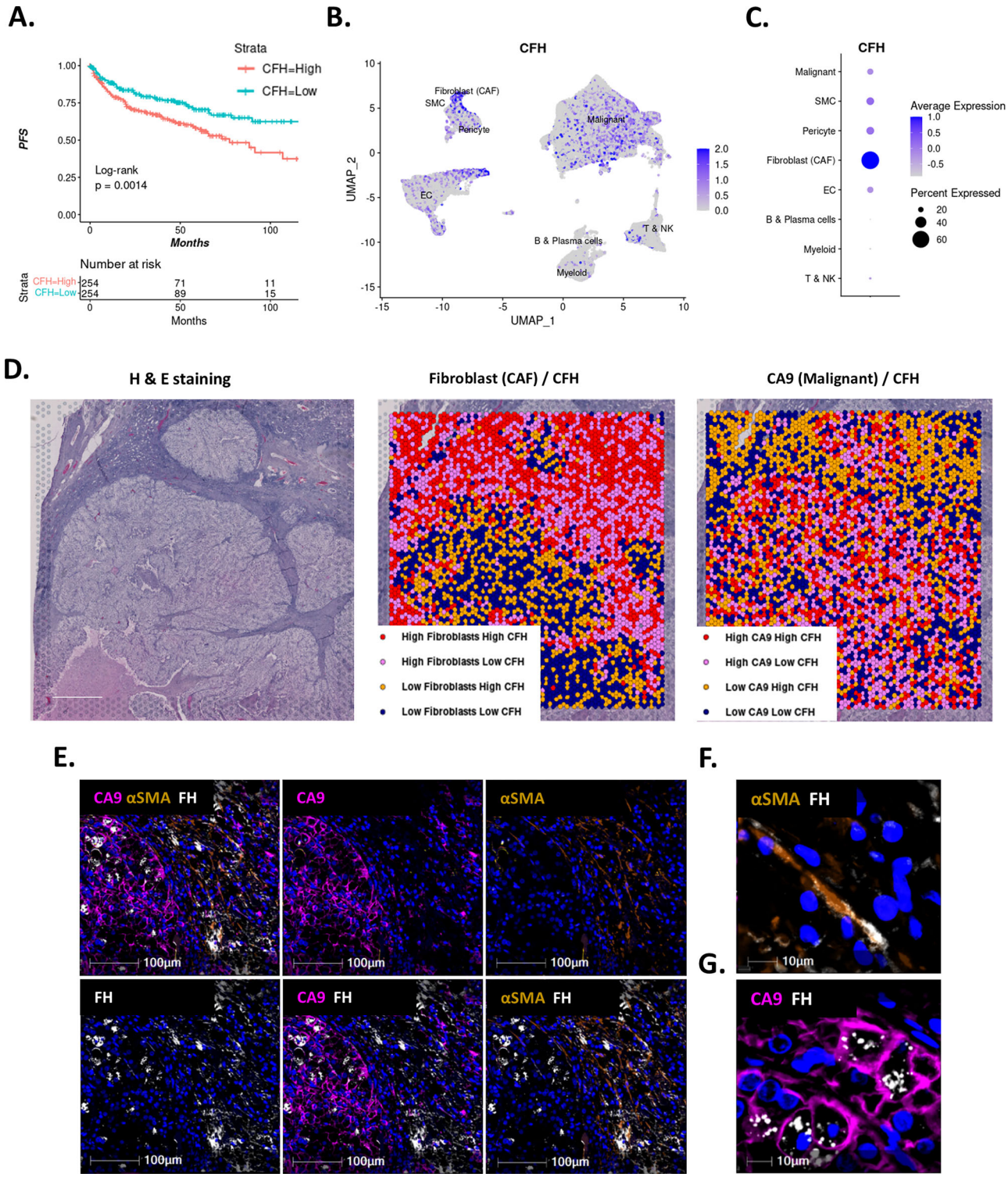

Fig. 1 | CFH is primarily expressed by fibroblasts and tumor cells, and its presence associates with poor prognosis in ccRCC. A Progression-Free Survival Kaplan–Meier curves according to *CFH* expression in the KIRC TCGA cohort ($n = 508$). **B** UMAP displaying *CFH* expression across labelled Seurat clusters from 20 different ccRCC primary tumors[25]. **C** Dot plot displaying *CFH* scaled mean expression levels (dot color) and percentage of cells (dot size) within each Seurat cluster. **D** Hematoxylin-eosin (H&E) section of a representative primary ccRCC tumor used for spatial transcriptomic analysis (left); Same section displaying labelled spots for *CFH* and fibroblast signature high and low categories (middle), or *CA9* high and low categories (right). Scale bar 1 mm. **E** Immunofluorescence of CA9 (pink), alpha-SMA (orange) and Factor H (white) of a ccRCC primary tumor. **F** alpha-SMA (orange) positive CAF presenting positive FH staining (white). **G** ccRCC cancer cells positive for CA9 (pink) and for FH (white) staining. **F**, **G** Nuclei are stained with DAPI (blue).

ionic strength, FH presented a dose-dependent binding to E2F3, CAPZB, TFDP1, CREB1 and its known interacting partner C3b (Fig. 3E). No interaction was observed for Pro-C1s which was used as a negative control (Fig. 3E). We further confirmed the FH interactions for the two top candidates, E2F3 and the capping complex (represented by CAPZB) by independent co-IP followed by western blot (Fig. 3F).

To further elucidate the characteristics behind the FH interactions observed by ELISA, we performed SPR experiments with the confirmed

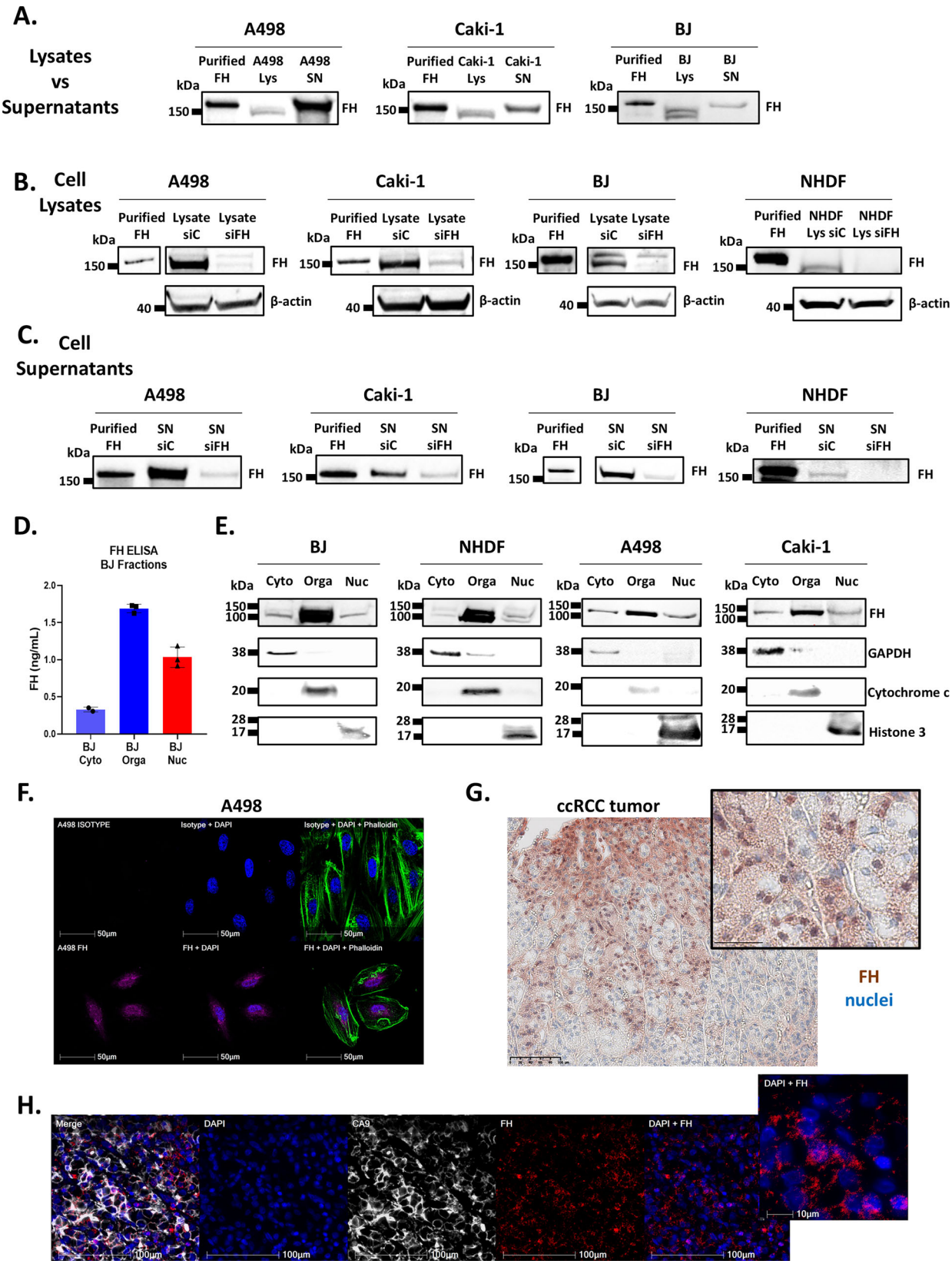

candidates at low and normal ionic strength conditions to study the contribution of electrostatic forces to the different interactions. At normal ionic strength, binding of FH to E2F3 was detectable by SPR (K_D ~ 110 nM) and was similar at low ionic strength (K_D ~ 265 nM) (Fig. 3G and Supplementary Table 4), making it the strongest binding partner revealed here. We did not detect FH binding to the other interacting candidates at normal ionic strength, but these were readily detectable under low ionic strength conditions, routinely used to explore FH binding properties[21–23]. Kinetics SPR analysis in this condition demonstrated that FH was able to bind also to CAPZB and CREB1 (Fig. 3F and Supplementary Table 4). Again, we

Fig. 2 | Cell intrinsic FH differs from secreted FH and it is located within various cellular compartments. A FH western blot with plasma purified FH along with lysates and SN from A498 and Caki-1 ccRCC cells (left and center, respectively), and BJ fibroblasts (right). **B** Western blot FH gene silencing validation in lysates from A498 cell (left), Caki-1 cells (center left), BJ fibroblasts (center right) and NHDF primary fibroblasts (right). **C** Western blot FH gene silencing validation in SN from A498 cell (left), Caki-1 cells (center left), BJ fibroblasts (center right) and NHDF primary fibroblasts (right). **D** FH quantification by ELISA on the different subcellular BJ fibroblasts' fractions. Average +/- SD, all data points are presented. **E** FH and compartment-specific proteins western blot for the different cell fractions in BJ fibroblasts (left), NHDF fibroblasts (center left), A498 cells (center right) and Caki-1 cells (right). Cyto = cytosol fraction, Orga = organelle fraction and Nuc = nuclear fraction. All gel images represent bands from the same experimental run, with separation into two boxes when unrelated intermediate lanes were present in the original blot. **F–H** Partial co-localization of FH with the nuclear staining: **F** Confocal microscopy evidencing staining for FH (red, rabbit anti-FH polyclonal, ProteinTech), the nuclear staining (DAPI, blue) and the actin cytoskeleton (phalloidin, green) in A498. **G** Chromogen staining by immunohistochemistry for FH (Ox24 monoclonal anti-FH, brown) and nuclei (blue) of a section of a ccRCC patient tumor. Scale bar of the main image – 100 µm and of the insert, 50 µm. **H** Immunofluorescent staining for FH (red, rabbit anti-FH polyclonal, ProteinTech), tumor cells (CA9, white) and nuclei (DAPI) in a section of a ccRCC patient tumor. **G**, **H** The inserts represent a zoomed image.

observed a robust interaction for the positive control C3b and absence of interaction in the negative control Pro-C1s (Fig. 3G).

Mapping FH binding domains using recombinant fragments (FH1-6, FH6-8Y, FH8-15, FH15-18, FH18-20 and FH19-20, Supplementary Fig. 8) showed preferential binding by FH6-8Y, followed by FH18-20 and FH19-20 across proteins under low ionic strength conditions (Supplementary Fig. 9 and Supplementary Table 5). Under physiological ionic strength, E2F3 also bound to FH6-8Y, but not FH18-20 or FH19-20 (Supplementary Fig. 9A, B).

Consistent with the SPR analysis, the intracellular FH interactome for the co-Ip with OX24 mAb (epitope: CCP5 of FH, between N-ter and central part fragments used for the SPR) revealed that E2F3 was not pulled down, aligning with the N-terminal FH interaction (Supplementary Fig. 7C). Interestingly, histones were observed for OX24 but not C18/3 mAbs Ips, suggesting a C-terminal interaction between FH and nucleosomes and/or genomic DNA (Supplementary Fig. 7C, D), as previously reported[22].

FH contributes to cell proliferation and survival through the regulation of p53 activity

As the FH interactome contained components of the Rb-E2F complex controlling cell cycle progression, we explored the effects of silencing *CFH* on the replicative capacity of fibroblasts. We observed that siFH-treated fibroblasts presented slower replication rates than siC cells (Supplementary Fig. 10A, B) as well as increased cell cycle arrest in the G0–G1 phase (Supplementary Fig. 10C). Notably, addition of exogenous FH into the culture medium did not restore the proliferative capacity of siFH fibroblasts (Supplementary Fig. 10D, E). Cell viability was also affected as indicated by an increased number of dead fibroblasts when *CFH* was silenced (Supplementary Fig. 10F, G). In agreement with our previous results[10], we also observed reduced viability and proliferation of siFH-treated ccRCC cells (Supplementary Fig. 10H–K).

The intranuclear presence of FH, along with its interaction with cell cycle transcription factors, led us to investigate the effects of silencing *CFH* on the fibroblast's transcriptome. siFH treatment of BJ cells resulted in upregulation of 155 genes and downregulation of 87 genes (Supplementary Fig. 11), consistent with the impact of siFH in the transcriptome of ccRCC cells[10]. To predict transcriptional regulators behind the induction/repression of these genes we employed ingenuity pathway analysis (IPA). Comparison across A498, Caki-1 and BJ cells revealed that the top 3 upstream regulators impacted by siFH were related to the regulation of the cell cycle. These included an increased activity for p53 (*TP53*) and reduced activity for aurora kinase (AURK) and anillin actin-binding protein (*ANLN*) which promote cell cycle progression (Fig. 4A). p53 is known to interact with various components of the Rb-E2F complex (Fig. 4B) to promote cell cycle arrest and apoptosis [39]. Paradoxically, *TP53* mRNA levels were not increased by siFH treatment (Fig. 4C), despite confirmation of the p53 signature by GSEA (Fig. 4D–F). Western blot analysis revealed accumulation and activation of p53 upon siFH treatment (Fig. 4G, H), suggesting that siFH leads to increased stabilization of p53 protein. Immunofluorescence further confirmed an increase in the percentage of p53-positive nuclei in siFH BJ (5.3% siC, 66.91% siFH, 1.81% siTP53, 1.01% siTP53+siFH, Chisq-test p-value < 0.01) and A498 cells (2% siC, 56.82% siFH, 0.14% siTP53, 1.87% siTP53+siFH, Chisq-test p-value < 0.01) (Fig. 4I). Signaling arrays on the siC vs siFH BJ lysates did not identify activity changes for other pathways such as JAK/STAT, MAPK, AKT, TGF-β and NF-kβ (Supplementary Fig. 12).

To investigate if the FH impact on cell proliferation was dependent of p53, we co-silenced *CFH* and *TP53* in BJ fibroblasts and A498 cells. Double silencing partially restored proliferation compared to silencing *CFH* alone in A498 cells, while in BJ fibroblasts, proliferation was fully recovered and even enhanced in the absence of *TP53* (Fig. 4J). Notably, a significant increase in mortality was observed exclusively in FH-silenced cells in both cell lines (Fig. 4J).

FH silencing impairs F-actin cytoskeleton organization and spheroid forming capacity of ccRCC cancer cells

The presence of F-actin-capping protein complex components in the FH interactome of A498 ccRCC cells but not in the BJ fibroblasts is in line with the disrupted actin cytoskeleton (with increased presence of cortical rings and disruption of actin stress fibers) revealed by phalloidin staining (Supplementary Fig. 13A) with morphological changes in cell circularity and solidity (Supplementary Fig. 13B). Specially for Caki-1 cells, the differences were also significant for Aspect Ratio (elongation) and roundness.

As disruptions in the actin cytoskeleton alter spheroid formation during the initial phases of aggregation and compaction[24], we investigated the spheroid-forming capacity of siFH cells. Indeed, sphere-formation was perturbed in siFH ccRCC cells, with delayed aggregation and compaction, especially for Caki-1 cells (Supplementary Fig. 13C), which may in part be related to the altered cell morphology. No such perturbations were observed for BJ fibroblasts (Supplementary Fig. 13C). Of note, actin gene expression was not altered between the siC and siCFH cells in our cell lines (siC vs siFH: log2FC = −0.2 & adj.p.value = 0.6 (A498), log2FC = −0.32 & adj.p.value = 0.13 (Caki-1); log2FC = -0.3 & adj.p.value = 0.47 (BJ)) in line with western blot results comparing siRNA treated cells (Supplementary Fig. 13D, E).

Interestingly, siTP53+siFH treatment in A498 ccRCC cells did not correct cell morphology, suggesting that this phenotype is independent of p53 activation (Supplementary Fig. 14A). Again, no differences were observed between different BJ fibroblasts' conditions (Supplementary Fig. 14B).

To understand whether FH and the capping complex proteins identified in the ci-IP experiment participate indeed together in the regulation of the morphology of the cells, we explored the double silencing of FH and CAPZB (Supplementary Fig. 15). Single silencing in both FH and CAPZB resulted in morphological changes in cell circularity and solidity (Supplementary Fig. 15A) and spheroid formation capacity (Supplementary Fig. 15B), but the double silencing did not have an additive effect, supporting the hypothesis that the two proteins are acting in the same pathway.

CFH malignant cell overexpression associates with poor prognosis and proliferative cancer cell states in patient tumors

Next, we explored whether *CFH* expression and its intracellular mechanisms influenced tumor cell development by reclustering malignant cells from a publicly available snRNA-seq dataset[25]. Five distinct malignant cell

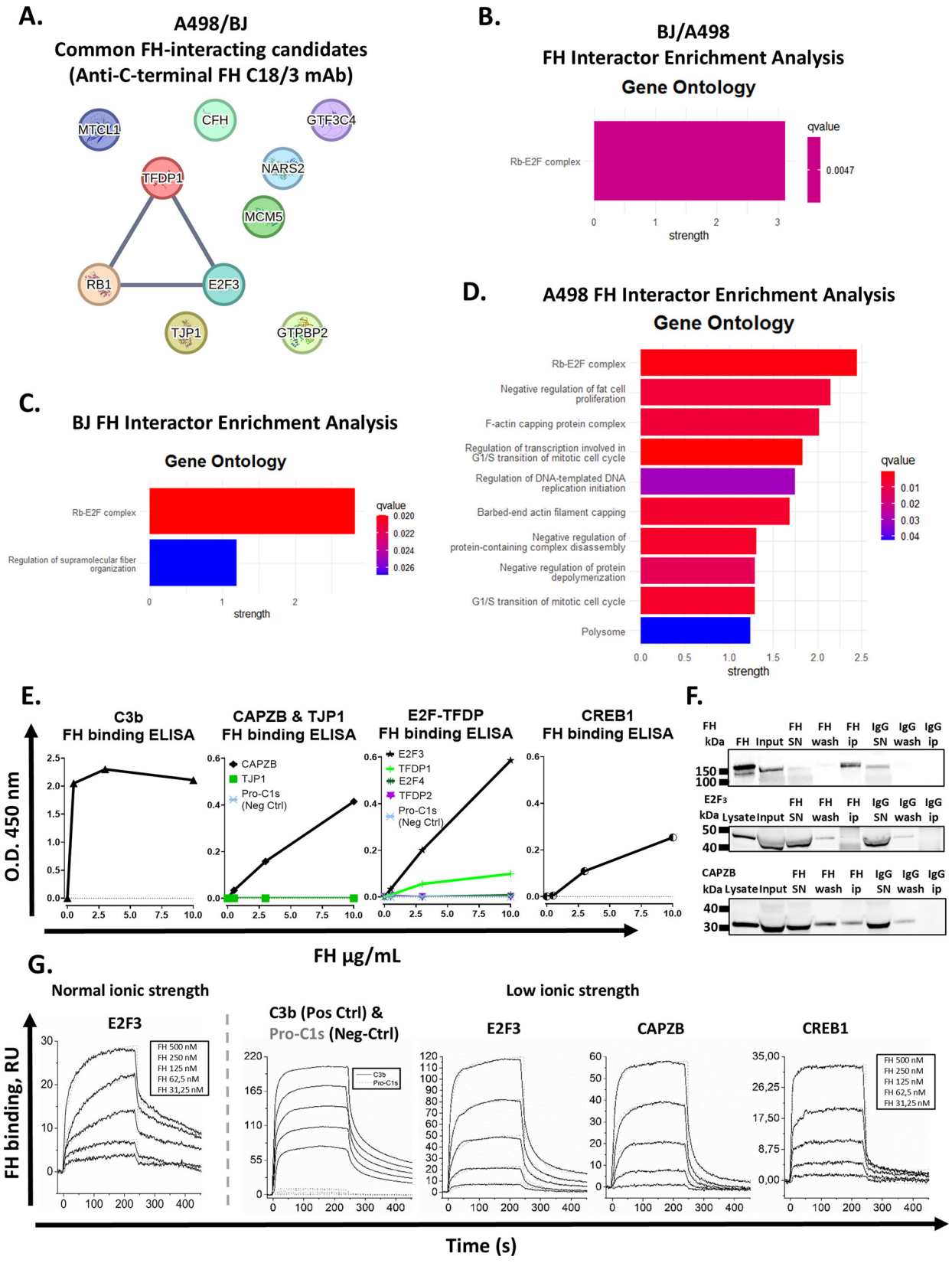

states with specific pathway enrichments (Fig. 5A–C and Supplementary Fig. 16) were identified throughout reclustering: an intermediate cancer cell state with a gradient for proximal tubular cell's signature "PT_Epi" (ccRCC_Int) (Fig. 5B), a proliferative cancer cell state enriched in DNA replication and cell cycle pathways (Cycling), a cancer cell state enriched in secretory pathways and EGFR signaling (EGF/EGFR_Secretory), a metabolically reprogrammed cell state enriched in mTORC1 signaling, glycolysis and oxidative phosphorylation (Metabolic), and an intermediate state between ccRCC_Int and Cycling cells enriched for Hedgehog signaling (Hedgehog) and high *CFH* expression (Fig. 5D).

Fig. 3 | Intracellular FH interacts with factors associated to F-actin capping and the Rb/E2F pathway. A Protein-protein interaction network analysis of common FH interacting proteins within A498 ccRCC cells and BJ fibroblasts (FH immunoprecipitated with anti-C-terminal FH mAb C18/3); STRING Tool, physical subnetwork with at least 0.4 confidence. Top 10 gene-ontology pathways for **B** the common FH interactors between A498 and BJ cells, **C** FH interacting candidates in BJ fibroblasts and **D** FH interactors identified in A498 ccRCC cells. **E** Protein-protein interaction ELISA dose-response analysis of purified FH binding to intracellular FH interacting candidates. **F** Validation of the co-immunoprecipitation of E2F3 and CAPZB together with FH. A498 lysate was incubated with anti-C-terminus FH mAb C18/3 (FH) or unspecific isotype control immunoglobuling G (IgG). Immunoprecipitation was then performed on protein A/G beads and proteins were eluted and probed by western blot for FH (upper line), E2F3 (middle line) and CAPZB (lower line). The validation of the target is based on its presence in the immunoprecipitates fraction with anti-FH (ip FH) but not in the one of the control IgG (ip IgG). Input: starting lysate material; SN: supernatant; ip: immunoprecipitates. **G** Kinetic SPR analysis using purified FH at concentrations ranging from 31.25 nM to 500 nM, twofold dilutions. FH was injected in normal (left) or low (right) ionic strength conditions on its respective FH interacting candidate coated chip for 240 s followed by 240 s dissociation. A 1:1 interaction with a drifting baseline curve was fitted to calculate kinetic parameters. The straight line represents the measured signal. The dotted one represents the kinetic fit. Curves from high to low RU values match the FH concentrations used (high FH, high RU values).

Next, we used Monocle3 to construct a pseudotime trajectory starting from the highest "PT_Epi" expressing cells in the ccRCC-Int cluster, representing an early cancer state resembling proximal tubular cells. Monocle3 algorithm revealed two main branches: "Branch 1", linking ccRCC_Int to Hedgehog and Cycling states, and "Branch 2" connecting ccRCC_Int to EGF/EGFR_Secretory and Metabolic states (Fig. 5E). Both branches shared enriched pathways across pseudotime reflecting processes such as epithelial-to-mesenchymal transition (EMT), response to inflammatory cytokines and hypoxia (Supplementary Fig. 17). Additionally, we identified branch-specific pathways such as E2F target gene expression associated to Branch 1 (Fig. 5F), while oxidative phosphorylation, protein secretion and p53 activation were enriched in Branch 2 (Supplementary Fig. 17). Notably, *CFH* expression (reflecting the Hedgehog cluster) rose along Branch 1 pseudotime, preceding a surge in proliferative genes like *MKI67* (Fig. 5G). Immunofluorescence staining of ccRCC tumors confirmed a significant Ki67 increase in FH-positive tumor cells compared to FH-negative cells (Fig. 5H, I).

Finally, we investigated the Hedgehog cell state abundance in the TCGA KIRC cohort using CIBERSORTx deconvolution based on our snRNA-seq references. Survival analysis revealed that high abundance of Hedgehog tumor cells associated with shorter OS (Fig. 5J).

CFH expression by fibroblasts is associated with poor patient prognosis in different cancer types

We identified a common intracellular FH mechanism modulating ccRCC and fibroblast cell proliferation, associated to ccRCC patient survival. These findings suggest that the pro-tumoral effect of FH may extend to other cancer types through its effects on fibroblasts. Analysis of scRNAseq datasets extracted from the Tumor Immune Single-Cell Hub revealed high *CFH* expression by cell clusters enriched in fibroblast signatures across most of the tumor types tested (Supplementary Fig. 18A). Next, we conducted a meta-analysis on the prognostic value of the *CFH* gene expression and MCP Counter cell signatures[26] across TCGA PanCancer cohorts. This analysis demonstrated that in all solid tumors where high *CFH* levels were associated with poor prognosis, fibroblasts signatures also correlated with poor patient prognosis (Supplementary Fig. 18B).

Discussion

Here, we report that fibroblasts and cancer cells express *CFH* under pro-inflammatory conditions, which associates with poor patient prognosis in ccRCC. However, FH is not a mere bystander of tumor inflammation. It acts intracellularly, by at least two independent mechanisms, to regulate fibroblast and cancer cell proliferation and actin polymerization in malignant cells (Fig. 5K). These data provide a paradigm shift on the impact of FH as a regulator of cancer hallmarks, showing how the pro-tumoral effect of FH stems from its intracellular functions.

In ccRCC tumors, *CFH* expression is carried out mainly by fibroblasts, followed by mural cells, endothelial cells and cancer cells. Even if FH protein staining was localized mainly in tumor cells[10], TCGA pan-cancer analysis revealed that the prognostic effect of *CFH* overexpression is closely linked to fibroblasts' signatures, the main source of *CFH* in various cancers. We also discovered a specific cancer cell state enriched for *CFH* expression that was also associated to poor clinical outcomes in the KIRC cohort. These findings suggest that FH contributes to tumor progression throughout both by its action in tumor cells and in fibroblasts.

FH is the master regulator of the alternative complement pathway C3 convertase (C3bBb)[27] and, in its canonical extracellular location, FH is expected to protect tumors from complement-mediated cytotoxicity and limit immune cell recruitment (by inhibition of C3a and C5a generation)[13]. In ccRCC, however, despite the upstream complement activation, there is no C5b-9-mediated tumor cell killing[28], C3 deposits are not associated with patient survival[29], and there is no correlation between intratumoral FH and immune infiltration[10]. Moreover, C3b and FB are below the detection limit in BJ, and we did not detect C3b in the FH interactomes. Supporting the role of intracellular FH in tumor growth, a recent report showed that *CFH* knockout tumor cells display reduced proliferation compared to wild-type cells in a CMT167 mouse model, without further inhibition of tumor growth when treated with an anti-FH mAb[12]. This aligns with our prior observations, where the absence of liver-derived plasma FH had no effect on tumor growth in a complement-sensitive TC-1-based mouse model[10,29]. Thus, the negative prognostic impact of *CFH* expression cannot be attributed to the canonical functions of the FH protein.

The higher expression of *CFH* in ccRCC tumors compared to normal tissue could be explained by the inflammatory nature of ccRCC[30]. Indeed, *CFH* synthesis in ccRCC tumors and cell lines correlated with the expression of the pro-inflammatory cytokine IL-6. IL-6 is associated with ccRCC tumor progression[31], partly through stimulation of EMT[32,33]. FH expressing ccRCC cancer cells in patients exhibit low cytokeratin and express the mesenchymal markers N-cadherin and vimentin[10]. Consistent with these observations, our trajectory analysis showed that both EMT and response to inflammatory cytokines, along with *CFH*, were increased across Branch 1 linking early tumor cell states to active proliferation. Therefore, the pro-tumoral FH functions could take place in cells that undergoing EMT and also in fibroblast, which are mesenchymal, but not in primary renal proximal tubule epithelial cells from which ccRCC originates[10].

Intratumoral FH overexpression has biological functions and is not a simple consequence of inflammation, as knocking down FH in vitro resulted in marked, coordinated changes in cancer cells and fibroblasts' transcriptomes. Strikingly, we found intracellular FH not only in the organelles and cytosol, but also in the nuclear compartment by cell fractionation and staining as well as in patient tumors, suggesting that it can regulate transcription of the differentially expressed genes. The nuclear localization can be explained by the presence of a NLS in the linker region between the CCP1 and CCP2 domains of FH which was hinted already in a previous report[34]. The intracellular FH exhibits a lower molecular weight than its secreted counterpart (observable also in images from a previous work[35]), suggesting that it is not reabsorbed, but rather synthesized and retained within the cell. This could explain why addition of purified FH to the cell media does not rescue the phenotype of siFH treated fibroblasts herein and ccRCC cells[10]. The decrease in molecular weight likely results from a lack of glycosylation, as the difference mirrors the 17.9 kDa mass decrease of glycosidase-treated FH[36]. We thus hypothesize that the presence and function of intracellular FH are intrinsic to its synthesis within the cell

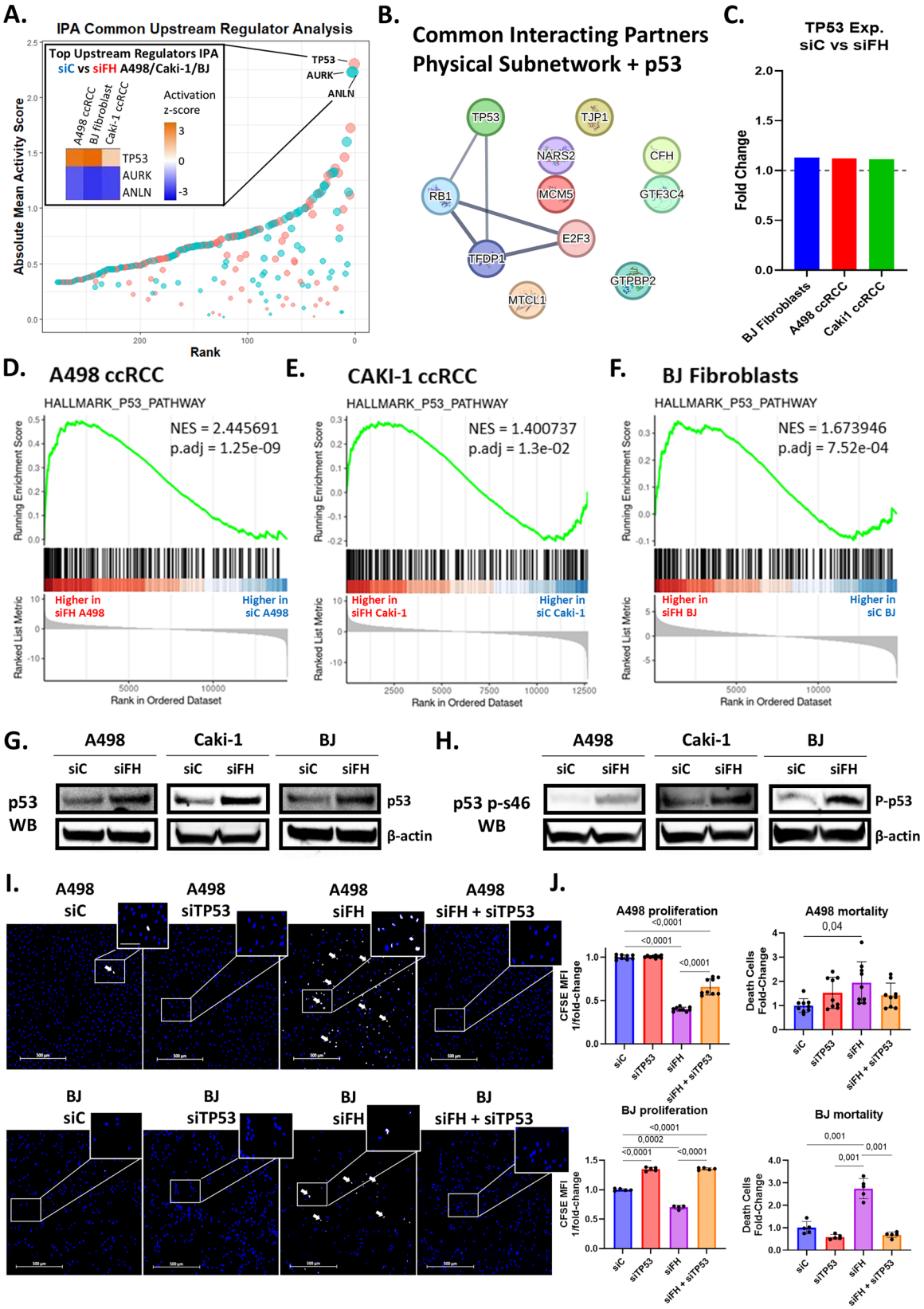

and are at least in part related to its nuclear localization and transcription control.

This hypothesis was supported by the observed interaction between intracellular FH and Rb/E2F complex transcription factors in A498 and BJ cells, as well as in RPE cells[37]. This complex is involved in the regulation of the cell cycle, during the G1/S transition[38], which aligns with the G0/G1 cell cycle arrest observed in siFH-treated fibroblasts here and previously for siFH ccRCC cells[10]. E2F family members E2F1, E2F2 and E2F3 contain a known binding site shared between cyclin A and p53. Binding of p53 to E2F1, E2F2 or E2F3 facilitates its nuclear retention[39] and apoptotic

Fig. 4 | CFH silencing increases p53 transcription factor activity and reduces ccRCC and fibroblast cell proliferation and viability. A IPA comparison analysis of common predicted upstream regulators in siFH vs siC treated A498, Caki-1 and BJ cells. Top 3 upstream regulators across cell lines are annotated and a heatmap with their activation z-score in siFH is presented. **B** Protein-protein interaction network analysis of common FH interacting proteins and p53; STRING Tool, physical subnetwork with at least 0.4 confidence. **C** *TP53* expression fold change (siFH/siC) for A498, Caki-1 and BJ cells. GSEA plots for the p53 pathway (hallmark gene set) comparing siFH vs siC treated **D** A498 ccRCC cells, **E** Caki-1 ccRCC cells and **F** BJ fibroblasts. Western blot analysis of **G** total p53 and **H** phosphorylated p53 S46 levels in the lysates of siC and siFH treated A498 ccRCC cells, Caki-1 ccRCC cells and BJ fibroblasts. **I** Immunofluorescence staining of p53 (light yellow) and nuclei (blue) of siC (left), siTP53 (left center), siFH (right center) or siTP53 + siFH (right) treated A498 cells (top row) and BJ fibroblasts (bottom row). Arrows indicate representative nuclei positive for p53 staining. The scale bar in the insert is of 100 µm and of the main image – 500 µm. **J** Evaluation of proliferation (left panels) and mortality (right panels) of siC, siTP53, siFH and siTP53 + siFH treated A498 (top row) and BJ (bottom row) cells. Cell proliferation is shown as inversed Fold Change of CFSE geometric means and mortality is represented as the Fold Change of DAPI stained dead cells. Exact *p* values indicated on the figures. Brown–Forsythe and Welch ANOVA tests plus *post-hoc* Tamhane's T2 multiple comparisons test.

function[40], but only when cyclin A levels are low before the S phase. Using a mAb anti-C terminus for FH, we co-immunoprecipitated E2F1 (in A498 cells only) and E2F3 (in both cell lines) in the absence of either p53 or cyclin A. It is possible that FH may interfere with p53 binding to E2Fs during the G1 phase, thus preventing p53 transactivation and cell death. Indeed, silencing *CFH* led to increased nuclear p53 accumulation, activation and transcriptomic activity in both fibroblasts and ccRCC cells, resulting in reduced cell proliferation and viability. Furthermore, co-silencing p53 along with FH completely reverted the phenotype observed for siFH fibroblasts and partly for siFH ccRCC cells. E2Fs transcription factors were not co-immunoprecipitated with an antibody against FH N-terminal CCP5 (OX24) likely due to competition/steric hindrance, suggesting that this part of FH interacts with E2Fs. Supporting this, we mapped by SPR the main E2F3 binding site to the FH fragment FH6-8. Interestingly, OX24-co-Ip FH pulled down histones, indicating a potential interaction between DNA and nuclear FH. Indeed, FH has been reported to interact with both histones[22] and DNA[22,41,42], the former interaction being mapped to the FH's C-terminal domain[22], in agreement with its loss when a high-affinity anti-C-terminal antibody C18 was used for the co-Ip. Together, these data support a hypothetical model in which DNA-bound nuclear FH limits p53 binding to E2F during the G1 phase through the interaction of the FH6-8 domains with E2F3, thus protecting cycling fibroblast and ccRCC cancer cells from p53-mediated apoptosis and cell cycle arrest. Proving this working model will require further studies.

Apart from the Rb-E2F complex, we found that FH interacts with capping complex proteins and TRIOBP in ccRCC cells, but not in fibroblasts. These proteins are involved in actin filament capping, cell motility and growth[43,44]. This interaction could explain why siFH ccRCC cells presented abnormal cell shapes, altered actin cytoskeleton, delayed spheroid formation, as well as why co-silencing of p53 and FH could not fully rescue the proliferative phenotype. Furthermore, we have already shown that siFH ccRCC cells present reduced cell migration[10]. Interestingly, it has been reported that $FH^{-/-}$ mice present an altered cytoskeleton of the muscle[45], of glomerular endothelial cells[46], and of the bone-marrow derived osteoblasts and osteoclasts[47]. Intracellular FH-positive cancer cells are also positive for mesenchymal markers[10], suggesting a more motile phenotype. At the molecular level, this cytoskeleton remodeling could be at least in part explained by the binding between FH and the capping complex in the cytosol, localized in the known charged pattern-binding domains CCP6-8 and CCP19-20[48], which may prevent excessive capping of actin filaments throughout competitive binding between actin filament barbed ends and FH. The exact mechanism of this process requires further investigation, but our data suggest that intracellular FH could be important in sustaining not only proliferation but also invasion and metastasis of cancer cells that have undergone EMT under pro-inflammatory stress.

Even if we could not extract pure CAF population from ccRCC tumors, consistent with the challenges reported by other groups[15,16], our results revealed concordant phenotype in (1) tumor cells, (2) in BJ fibroblasts expressing CAF markers such as α-SMA and FAP[18,19] known to be associated to cancer progression and immunotherapy resistance in ccRCC[11], and (3) in normal fibroblasts (NHDF). Unlike previous phenomenological studies[49], our molecular mechanisms discovered here could explain FH depletion phenotypes in other cell types such as RPE cells[50], glomerular endothelial cells[46], osteoblasts and osteoclasts[47]. Recent work on glomerular mesangial cells in IgA nephropathy further supports FH's role in cell cycle progression and actin cytoskeleton maintenance via transcriptomic changes[51], though the underlying mechanism was not explored using rescue experiments. Our findings provide a possible explanation, as their transcriptomic data showed upregulated p53 signaling[51]. Therefore, the biological relevance of intracellular FH is not limited to cancer, and its dysregulation may explain disease activity related to other cell types in rare diseases such as FH-deficiency associated atypical hemolytic uremic syndrome and glomerulopathies or to FH-genetic polymorphism-associated age-related macular degeneration.

High FH expression in the ccRCC tumor environment and the favorable prognosis associated with autoantibodies[28] against the form of FH targeted by GT103[7,12–14,52–56] suggest ccRCC as a promising candidate for this therapy. Since intracellular FH may evade treatment, it's worth exploring if responders will show membrane FH staining related to complement cascade, while non-responders show none or only intracellular FH, linked to cell cycle control.

Taken together, our results shed light on novel FH-mediated mechanisms which promote tumor progression through modulation of cancer hallmarks related to proliferation in cancer cells and fibroblasts. We propose a model in which FH interacts with key regulators such as the Rb/E2F complex and actin capping protein complex, which could influence transcriptional activity of cell cycle regulators and cytoskeleton architecture.

Methods

Bioinformatic analysis of publicly available datasets: snRNA & scRNA-seq

snRNA-seq data from ccRCC primary tumors and normal adjacent tissue was taken from Hu et al.[25,57]. The data was processed as indicated in the original publication, and analyzed using R (R version 4.3.2) and the "Seurat" package. Cell annotations were as provided by the authors. The "presto" package was used to obtain differentially expressed genes (DEGs) between *CFH* high and *CFH* low (median expression) fibroblasts and malignant cells. All genes were ranked by their log2 fold changes within the positive *CFH* group and used as input for preranked GSEA ("fgsea" method) using the "clusterProfiler" package[58] and the hallmark gene sets from the molecular signature database[59].

All malignant cells were employed for reclustering. Misclustered cells were removed based on broad labeling, and data were normalized, scaled, and reclustered at increasing resolutions to optimize subcluster identification. Cell cycle effects were retained to assess *CFH* impact on proliferation. Annotations were based on enriched pathways via Over representation analysis (ORA) on DEGs (avg_log2FC>log2(1) & *p*.val.adj<0.05) employing "SCP" package.

We used "Monocle3" to infer paths between malignant cell states across differentiation and cell cycle. The Seurat object was converted to a Monocle object using "SeuratWrappers" package, and cell subclusters were partitioned, with a trajectory fitted to the biggest partition containing all the cancer cell states. The root was determined by identifying expressing cells for a proximal tubular cell signature "PT_Epi" (CellMarker 2.0 database[60]). DEGs across pseudotimes were calculated using "graph_test()" with

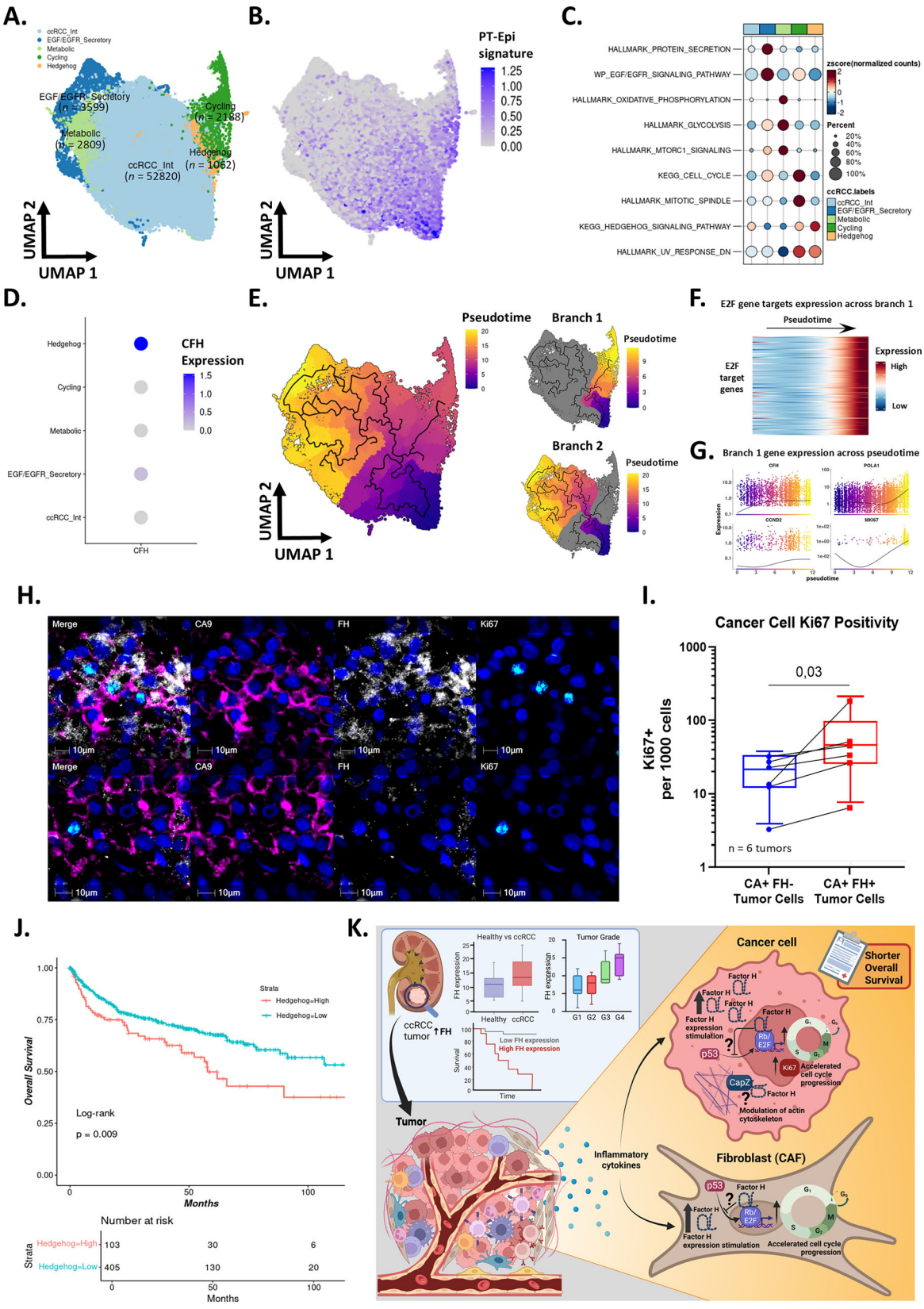

"neighbor_graph" set to "principal_graph" (q.value < 0.05) and ORA was performed using "SCP" package.

To study the single cell expression of *CFH* across cancers, data was extracted from the Tumor Immune Single-Cell Hub (http://tisch.comp-genomics.org/, accessed 04/02/2024)[61] :UCEC_GSE139555, STAD_GSE134520, SKCM_GSE115978, PAAD_CRA001160, OV_GSE118828, NSCLC_GSE131907, NHL_GSE128531, NET_GSE140312, MCC_GSE117988, LIHC_GSE125449, KIRC_GSE111360, HNSC_GSE103322, CRC_GSE146771, CHOL_GSE125449, BRCA_GSE138536 and BCC_GSE123813.[62]

Fig. 5 | Trajectory analysis of ccRCC malignant cells reveals a CFH enriched cell state associated with proliferation path and poor patient prognosis. UMAP displaying **A** the malignant cell states identified by reclustering, and **B** the proximal tubular cell signature expression across malignant cells. **C** Dot plot displaying significantly enriched pathways across malignant cell states, scaled mean expression levels (dot color) and percentage of cells (dot size). **D** Dot plot displaying *CFH* scaled mean expression levels (dot color) across malignant cell states. **E** Pseudotime trajectories of malignant cells inferred by Monocle3. Two main branches were identified: Branch 1 representing cells undergoing cell cycle progression, and Branch 2 representing cancer cell differentiation. **F** Expression of E2F target genes along the trajectory of Branch 1. **G** Expression of *CFH*, *POLA1*, *CCND2* and *MKI67* genes along the trajectory of Branch 1. **H** Immunofluorescence of CA9 (pink), Factor H (white) and Ki67 (light blue) of a ccRCC primary tumor. Representative Ki67 and FH positive (top row), and Ki67 and FH negative (bottom row) cancer cell staining. **I** Evaluation of Ki67 positive cell frequency in FH positive versus negative ccRCC cancer cells. The exact *p* value is indicated on the figure. Wilcoxon matched-pairs signed rank test. **J** Overall Survival Kaplan–Meier curves according to Hedgehog cancer cell signature abundance in the KIRC TCGA cohort ($n = 508$). **K** Proposed mode of action of intracellular FH in ccRCC fibroblasts and cancer cells. Created in BioRender. Roumenina, L. (2025) https://BioRender.com/gtfgxgw.

Bioinformatic analysis of publicly available datasets: Bulk RNA-seq

Gene expression (RNASeqV2) and clinical data from The Cancer Genome Atlas (TCGA) PanCancer cohorts were obtained through the "cBioPortalData" package[63]. Cell abundance was computed using the "MCPcounter" package[26] and scores were transformed into z-scores for each dataset individually. *CFH* expression was also z-transformed. The prognostic effects of each MCPcounter scores and *CFH* expression were evaluated by univariate Cox proportional hazards models fitted for Overall Survival using the "survival" package. Results were represented as the minus log10 coefficient's FDR adjusted *p*-values (Benjamini–Hochberg/BH method) multiplied by their corresponding log-transformed Hazard Ratio signs.

To study clinical associations between ccRCC and *CFH* expression and its correlations to immune-related receptor ligands, data were obtained from TCGA. *CFH* expression in normal and tumor tissue was compared by Mann Whitney test while expression across Tumor Stage and Tumor Grade were assessed by Kruskal Wallis test. *CFH*'s prognostic effect was evaluated using z-score transformation and multivariate Cox models adjusted for age, sex, Tumor Stage, and Grade fitted for Overall Survival and Progression-Free Survival (PFS). Kaplan–Meier curves were generated with "survminer" using median cut-off values. Hedgehog cell state prognostic impact was assessed via CIBERSORTx to estimate cell abundancies and Kaplan–Meier analysis with the CIBERSORTx scores at optimal cut-off. *CFH* correlations with immune mediators were analyzed using HUGO-listed gene groups (Interleukins (Group 601), Chemokines (Group 483), Interferons (Group 598), Tumor necrosis factor superfamily (Group 781) and Transforming growth factor beta family (Group 1664)) and visualized as correlation networks via "qgraph." Significant correlations ($|\text{Spearman's rho}| > 0.45$, BH $p.\text{adj} < 0.05$) were retained.

CFH and *IL6* expression across Renal Cell Carcinoma cell lines was studied by spearman correlation. Data was sourced from "OmicsExpressionProteinCodingGenesTPMLogp1.csv" ("DepMap Public 23Q4" on The Broad Institute Cancer Dependency Map Portal, https://depmap.org/portal/, accessed on 12 March 2024).

Bioinformatic analysis of publicly available datasets: Spatial Transcriptomics

A ccRCC spatial transcriptomic dataset [20], GSE175540[64], was processed using the "Seurat" package by discarding spots with more than 30% of mitochondrial genes and keeping spots with at least 300 genes. Genes detected in less than 5 spots were removed. Counts were normalized using "SCTransform()" with the "assay=spatial" parameter. Cell abundance scores estimated with "MCPcounter" and *CFH* expression were dichotomized into "high" and "low" spots according to median cut-off, with the same approach applied to *CA9* for tumor detection. Co-localization between *CFH* and MCP score labels was evaluated by a two-sided Fisher's exact test, and Odds Ratio and significant association frequency across slides were reported as a barplot using "ggplot2". Representative co-localization was shown using the "SpatialDimPlot()" function and the localization of "high-high" spots.

ccRCC tissue staining with automated multiplexed sequential immunofluorescence (seqIF)

FFPE tissue blocks from primary ccRCC tumors were obtained from the commercial source France Tissue Bank and no ethical approval was needed for this research. These archived tissue samples were anonymized prior to access through the researchers. All ethical regulations relevant to human research participants were followed. The seqIF was performed using the COMET platform (Lunaphore Technologies). The multiplexed panel comprised 4 antibodies targeting FH (anti-Factor H, ProteinTech 12748-1-1P), Ki67 (anti-Ki67, Dako 7240), CA9 (anti-Carbonic anhydrase 9, Abcam ab243660), and α-SMA (anti-alpha smooth muscle actin, Dako M0851) (Supplementary Table 1). Secondary Alexa fluorophores 555 (A32727, ThermoFisher Scientific) and 647 (A32733, ThermoFisher Scientific) were used at 1:200 and 1:400 dilutions, respectively. Image analysis were performed with Halo10 software (Indica Labs).

Cell lines

Primary Normal Human Dermal Fibroblasts (NHDF, Promocell C-12302), the human dermal fibroblast cell line BJ (ATCC CRL-2522) and two ccRCC cell lines (A498 and Caki-1, ATCC HTB-44 & HTB-46, respectively, both p53 wild type, the first being VHL mutated, but not the second one) were employed. NHDF cells were cultured in Fibroblast Growth Medium 2 (Promocell C-23020) + x1 Supplement Mix Fibroblast Growth Medium 2 (Promocell C-39325). Caki-1 cells were cultured in McCoy medium (ATCC 30-2007) + 10% heat-inactivated FCS (Eurobio Scientific CVFSVF00-01) + 1× penicillin/streptomycin (Gibco 15140-122). A498 cells and BJ fibroblasts were cultured in Eagle Minimum Essential Medium (ATCC 30-2003) + 10% heat-inactivated FCS + 1× penicillin/streptomycin + 1× HEPES (Gibco 15630-080). All cell lines were cultured in a humidified atmosphere of 5% CO_2 at 37 °C and routinely tested for Mycoplasma (Lonza LT07-318). Primary NHDF cells and BJ fibroblasts were used up to four passages, while the tumor cell lines were used up to 20 passages. All cells were routinely authenticated by morphology.

Cytokine stimulation

A498, Caki-1 and BJ fibroblasts were plated in 6-well plates with 2 mL of OptiMEM (Gibco 31985-062). Cytokine stimulation was performed in duplicates with either 10 ng/ml of TNF-α (R&D Systems 210-TA), 10 ng/mL of IL-1β (Peprotech 200-01B), 10 ng/mL of IL-6 (Peprotech 200-06), 10 ng/mL of TGF-β1.2 (R&D Systems 304-B3) or media alone for 24 h. Cell supernatants and cell lysates were collected for subsequent measurements.

FH ELISA

FH levels in lysates, cell fractions and supernatants were measured by ELISA as previously described[10,65]. Results are expressed in ng/mL according to the standard curve (4PL curve fit) prepared by serial dilution of purified FH (CompTech A137). Cytokine-stimulated supernatant results are expressed as fold change from the non-stimulated control.

Quantigene

Cells were used to directly quantify the RNA transcripts of FH utilizing a custom-designed QuantiGene Plex Gene Expression Assay according to

manufacturer's instructions. The multiplex panel included complement (CFH, C3AR1, C2, C5AR2, C1S, C5AR1, C7, C5, CFB, C1R, C3, C4A, C4B) and reference genes (HPRT1, GUSB, RPL19, POLR2A). Signal detection was performed with Luminex FLEXMAP 3D Instrument System (ThermoFisher). Data was normalized by dividing mean fluorescence values over housekeeping genes and compared to the corresponding non-stimulated cells.

Gene silencing

Cells were transfected with a pre-incubated siRNA mixture (30 min, room temperature) containing: 4 *CAPZB* siRNAs (Qiagen GeneSolution GS832), or 2 *CFH* siRNAs (Qiagen SI00003983 and SI00003990), or 1 *TP53* siRNA (Qiagen SI02655170), or siRNA control (Qiagen SI03650318), or 2 *CFH* siRNAs + 1 *TP53* siRNA or 4 *CAPZB* siRNAs + 2 *CFH* siRNAs (for double silencing) at 50 nM each with lipofectamine RNAimax (ThermoFisher 13778150) in OptiMEM. Silencing was performed at 50% confluence in 6-well plates, 10 cm^2 petri dishes or T75 flasks, and stopped after 24 h. Immunofluorescence and functional assays were performed 96–120 h post transfection.

Secretome array

Cytokines present in supernatants from 96 h post transfection of siC or siFH BJ fibroblasts incubated in OptiMEM were measured by Human Cytokine Array Q1000 (RayBiotech QAH-CAA-1000) according to manufacturer's instructions. Only cytokines above the OptiMEM media alone (negative control) were considered secreted by the cell line and reported.

Western blot analysis

Lysates (prepared in RIPA buffer, Abcam ab156034, supplemented with protease inhibitors, Roche 11836145001, and phosphatase inhibitors, Roche 04 906 837 001), supernatants of cells cultured in OptiMEM for 96 h, and cell fractions (prepared with Abcam ab109719) were employed for Western Blot. Supernatants were adjusted based on cell counts and lysates based on protein concentration assessed by Bradford assay. Samples were mixed with NuPAGE LDS buffer (±DTT), denatured at 90 °C for 5 min, and loaded onto 4–12% or 10% Bis-Tris gels (Invitrogen NW04122BOX, NW00100BOX), depending on the antigen detected (see Supplementary Table 2; anti-Factor H (Quidel A312), anti-β-actin (ThermoFisher Scientific MA1-140), anti-GAPDH (Proteintech, 60004-1-Ig), anti-cytochrome c (Proteintech, 66264-1-Ig), anti-Histone 3 (Proteintech 17168-1-AP), anti-p53 (SantaCruz, sc126), anti-p53-phosphorylated-s46 (R&Dsystems mAb1489), anti-E2F3 (Proteintech, 27615-1-AP) and anti-CapZ-β (Proteintech, 25043-1-AP)). Proteins were transferred onto nitrocellulose membranes (Invitrogen IB23001), blocked using 5% BSA w/v tris-buffered saline (TBS) and incubated overnight at 4 °C with primary antibodies (Supplementary Table 2). Purified FH (CompTech A137) or cell material from silenced cells were used as positive and negative controls. Primary antibody binding was detected by incubation with the corresponding HRP-conjugated secondary antibody (Supplementary Table 2) and chemiluminescence using a substrate for HRP (Thermo Fisher Scientific 34076) and detected by iBright Western Blot Imaging System (iBright™ CL1500 Imaging System, Thermo Fisher Scientific). The uncut images of the western blots are presented in the Supplementary Information Uncut gels section.

In silico visualisation of the NLS sequence

The three-dimensional coordinates of the FH CCP1-CCP4 were extracted from the Protein Data Bank, 2WII[66] using PyMOL (http://www.pymol.org/), and the visualization was performed using Discovery Studio visualizer (Biovia, D.S).

Co-Immunoprecipitation for mass spect and bioinformatic analysis

Cells were grown for 48 h, washed with cold PBS and harvested by scraping with IP lysis buffer (0.5% NP40 (Sigma N-6507), 1× Complete protease inhibitor (Roche 11836145001), 1% v/v Phosphatase Inhibitor Cocktail 2 (Sigma-Aldrich P5726) and 1% v/v Phosphatase Inhibitor Cocktail 3 (Sigma-Aldrich P0044)). Co-immunoprecipitation was performed with 2 mg of lysate protein using 4 µg of anti-FH mAbs (OX24 kind gift from Pierre Fabre Research Institute, or C18/3 Santa-Cruz sc-47685) or IgG control (Santa-Cruz sc-2025). Lysates were incubated with their respective antibodies (1 h, 4 °C) before addition of 80 µL of Protein A/G PLUS-Agarose beads (Santa-Cruz sc-2003) for incubation overnight at 4 °C under agitation. Beads were then washed with IP washing buffer (0.1% NP40 (Sigma N-6507), 1% Phosphatase Inhibitor Cocktail 2 (Sigma-Aldrich P5726) and Phosphatase Inhibitor Cocktail 3(Sigma-Aldrich P0044)), and proteins were eluted with acidic glycine buffer (200 mM, pH = 2) and neutralized with TRIS buffer (1 M, pH = 8.5). Eluted proteins were stored for Western Blot validation or processed for protein precipitation with methanol/chloroform[67]. The mass spectrometry analysis was performed following the protocol described by Merle et al.[37]. Statistical analysis (anti-FH vs. IgG control) was performed using Perseus[68], with imputation for NaN values. Significantly enriched proteins ($p < 0.01$) were identified via Significance A test on log2 Fold Changes, and gene ontology/protein interaction networks were analyzed using STRING Tool[69].

Protein-protein interaction ELISA

Nunc MaxiSorp ELISA plates (Thermo Fisher Scientific 439454) were coated overnight at 4 °C with 50 µL/well of 0.2 µM target proteins (CREB1 CreativeBiomart CREB1-26H, TJP1 OriGene TP322836, CAPZB OriGene TP310480, E2F3 CreativeBiomart E2F3-27375TH, E2F4 Abcam ab152352, TFDP1 CreativeBiomart TFDP1-1412H, TFDP2 OriGene TP760154) or controls (C3b as positive, Pro-C1s as negative CompTech A114 & A103). Wells were blocked with 2% BSA in PBS (1 h, 37 °C) and incubated with purified FH (0–10 µg/mL, Quidel A410) in Hepes buffer (10 mM Hepes, 150 mM NaCl, 0.05% v/v Tween20) for 1 h at 37 °C. Binding was detected using a biotinylated anti-FH antibody (3.6 µg/mL, 1 h, 37 °C), followed by streptavidin-HRP (1:500, Dako P0397) for 30 min at 37 °C. Signal was developed with SureBlue TMB substrate and read at 450 nm using the Infinite 200 PRO (Tecan).

Surface plasmon resonance

The kinetic constants of the binding between FH and the different intracellular FH-interacting candidates were determined by SPR technology with BIAcore 2000 equipment (Cytiva Life Sciences, Biacore) using the proteins employed in the Protein-protein interaction ELISA. Recombinant proteins were coupled to a CM5 sensor chip using amine coupling, with efficiencies of 3000 RU (E2F3), 1000 RU (CAPZB), and 3500 RU (CREB1). C3b and Pro-C1s were used as positive and negative controls, respectively, at 1000 RU.

All binding experiments were performed at flow rate of 10 µL/min with a temperature of 25 °C, with FH (500 to 31.25 nM) injected in normal (0.01 M HEPES pH 7, 0.15 M NaCl, 0.005% v/v Tween20; 0.22 µm filtered and degassed) or low ionic strength (0.01 M HEPES pH 7, 0.05 M NaCl, 0.005% v/v Tween20; 0.22 µm filtered and degassed) buffers. The association and dissociation phases were followed for 4 min each. 5 µL of 1 M NaCl 0.05 M NaOH regeneration buffer were employed between different FH dilutions. For domain mapping, various FH recombinant fragments (FH1-6, FH6-8Y, FH8-15, etc.) were used[70,71] at different concentrations ranging from 500 to 15.62 nM or 250 µM to 7.8 nM diluted in either normal or low ionic strength buffers. Data were analyzed using BIAevaluation software (version 4.1; Biacore, GE Healthcare), and the binding to the empty chip sensor surface was subtracted to estimate the kinetic binding constants. Kinetic parameters were determined using a 1:1 interaction model with a drifting baseline. Binding responses were visualized using Origin software(version 6.1; OriginLab).

Immunofluorescence

48 h post transfected BJ fibroblasts and A498 ccRCC cells (30,000 cells per cover glass) were cultured for 2 days, fixed with 4% PFA, permeabilized with 0.1% Triton X-100, and blocked with 1% BSA at room temperature for 1 h.

Cells were stained with 1:50 α-p53 mAb (SantaCruz sc126) or anti-FH OX24 (Mouse, expressed in house) or anti-FH rabbit polyclonal (Proteintech, ref 12748-1-AP) or isotype controls (Dako FLEX negative control mouse and rabbit cocktail, catalog no IR750 and IR600 respectively) overnight at 4 °C, and then with Phalloidin-IFluor 488 reagent (Abcam ab176753) for 90 min in the dark. After incubation with 1:200 α-mouse-AF55 (Lunaphore Technologies DR555MS) or Alexa Fluor 555-conjugated Goat anti-Mouse IgG (Invitrogen, ref A-21422) or Alexa Fluor 647-conjugated Goat anti-Rabbit IgG (Invitrogen, A32733TR) secondary antibodies and 1:500 of DAPI (Thermo Fisher Scientific 62248), slides were mounted with ProLong™ Diamond Antifade Mountant reagent (Thermo Fisher Scientific P36961) and scanned with AxioScan (Zeiss).

Confocal images and Z stacks were obtained with Leica Stellaris 5 (Leica Microsystems). The image processing and analysis were performed with ZEISS ZEN lite (ZEISS) and Halo10 (Indica Labs) software. For the morphological analyzes, images were contrast-normalized (CLAHE), converted to 8-bit, and segmented using Huang's automatic threshold (with smoothing). Binary masks were analyzed with Analyze Particles (size filter 100–10,000 px), with Set Measurements configured for Area and Shape descriptors. The exported per-cell measurements included: Circularity, Aspect Ratio (AR), Roundness, and Solidity. Per-cell values were compared between conditions using two-sided Mann–Whitney U tests.

The % of FH staining present in the nucleus vs the cytoplasm was analyzed on the confocal microscopy images (single optical plane) using HALO AI software. Four fields of view of FH-stained A498 cells were included for quantification. Whole-cell boundaries were manually annotated using actin staining, and nuclei were delineated based on DAPI. FH-positive area was quantified in each annotated region using the Area Quantification FL module. The cytoplasmic FH area was obtained by subtracting the nuclear FH area from the whole-cell FH area. The proportion of FH localized to each compartment was calculated as the FH area within that compartment divided by the total FH area (nucleus + cytoplasm).

RNA sequencing (RNAseq)

The RNAseq experiments were performed by the GenomIC Cochin Institute INSERM U1016. Samples were prepared in quadruplicates. BJ cells were transfected (siC vs. siFH) and cultured for 5 days before RNA extraction using the Maxwell® 16 LEV kit (Promega AS1270). RNA quality was evaluated with the Agilent 2100 Bioanalyzer system and 2100 Expert software. RNA integrity numbers for all samples were above 8. Libraries were prepared following the Stranded mRNA Prep protocol from Illumina, starting from 250 ng of high quality total RNA. Paired-end (2 × 51 bp) sequencing was performed on an Illumina NovaSeq platform. FASTAQ files were aligned using STAR algorithm (version 2.7.6a), on the Ensembl release 101 reference. RSEM (v1.3.1) was used for quantification, and the statistical analyzes on the read counts were performed with R (version 3.6.3) and the DESeq2 package (DESeq2_1.26.0)[72]. DESeq2's median of ratios normalization was used with a pre-filter of genes (at least 10 reads in at least 3 different samples). Wald test with the contrast function was employed in combination with the Benjamini–Hochberg FDR to identify DEGs (absolute log2-fold change > 1 and FDR adjusted p-value < 0.05).

In order to search for common transcriptionally enriched pathways between the three different cell lines (A498, Caki-1 and BJ), we employed gene expression data previously generated[10]. Identification of upstream transcriptional regulators commonly altered upon *CFH* silencing was performed by a combination of *Upstream Regulator Analysis* and *Comparison Analysis* using Ingenuity Pathway Analysis (IPA, Qiagen) on DEGs between siC and siFH treated cells. GSEA was performed using the "GSEA()" function from the "clusterProfiler" package[58] with the "fgsea" method on the list genes ranked according to the test statistic from the Wald test.

Proliferation and mortality assay

48 h post transfected cells were incubated with CFSE reagent 1:500 (Invitrogen C34554) for 30 min at 37 °C. Next, cells were cultured in 6-well plates for 48 h in the presence of the standard culture medium of each cell. On the day of flow cytometry acquisition, supernatants containing dead cells and trypzynised adherent cells were recovered, washed and stained with 1:1000 DAPI (Thermo Fisher Scientific 62248) for 10 min at room temperature. BD LSRFortessa (BD Biosciences) was employed for acquisition, and data were analyzed using FlowJo V.10.8.1 software. The gating strategy was on the cell population, doublets exclusion, identification of the live and death cells via DAPI, and their quantification as % of the total population, followed by determination of the geomean of the peak of CFSE staining on the live cells. The gating strategy is presented in Supplementary Fig. 19.

Phosphorylation pathway profiling array

The impact of silencing FH on BJ signaling pathways was studied by Human Phosphorylation Pathway Profiling Array C55 (RayBiotech AAH-PPP-1), following manufacturer's instructions on 120 h post transfection BJ fibroblast's (siC vs siFH) lysates. Spot intensities were quantified by ImageJ software.

Cell cycle

48 h post transfected BJ cells were fixed in ice-cold 70% ethanol and stored at −20 °C. On the day of cell acquisition, cells were stained with 50 µg/mL of propidium iodide (Invitrogen P1304MP) with 1:50 RNase (Thermo Fisher Scientific EN0601) for 30 min at room temperature. BD LSRFortessa (BD Biosciences) was employed for acquisition and cell cycle analysis was performed with FlowJo V.10.8.1 software, using the Watson (pragmatic) model.

Spheroids

24 h post transfection (siC vs siFH), A498, Caki-1, and BJ cells were seeded (10,000 cells in 50 µL) in 96-well cell-repellent plates (Greiner Bio One 650970). After overnight incubation, 150 µL of medium was added. Spheroid growth was monitored hourly and stopped 48 h after seeding. The same protocol was used for the spheroids formation for siC vs siFH vs siCAPZB vs siFH+CAPZB.

Statistics and reproducibility

Unless otherwise stated, statistical analysis was performed as follows: Kruskal–Wallis test (non-normally distributed data) or Brown–Forsythe and Welch ANOVA (normally distributed data) for associations between categorical and continuous variables, followed by specifically mentioned post-hoc tests in the figure legend. Spearman test was used for correlations between two continuous variables, and Fisher's exact test for two categorical variables. Log-rank test compared Kaplan–Meier curves. ORA used hypergeometric tests with corresponding gene backgrounds. Chi-squared test evaluated p53-positive nuclei across different silencing conditions. Welch t-tests assessed differences in cell cycle, proliferation, and mortality between siFH and siC cells. One-sample t-test was used for signalome array analysis. P-values were adjusted using the Benjamini–Hochberg method. Data are presented as means ± SD. The majority of the experiments were repeated at least in triplicate. Statistical significance: $^{*}P < 0.05$; $^{**}P < 0.01$; $^{***}P < 0.001$; $^{****}P < 0.0001$.

Reporting summary

Further information on research design is available in the Nature Portfolio Reporting Summary linked to this article.

Data availability

RNA-seq data is available on Zenodo (10.5281/zenodo.12795704) with a copy at GEO: GSE317434: https://www.ncbi.nlm.nih.gov/geo/query/acc.cgi?acc=GSE317434. Full raw data, search engine outputs, FASTA files, spectral library and necessary metadata and parameters settings of search engines, have been submitted and made publicly available at the Massive Proteomics repository (A full member of the ProteomeXchange consortium for proteomics data submission and dissemination), under the access codes: MassIVE MSV000100813 and MSV000100872, and accessible via

ProteomeXchange under PXD074376 and PXD074561. Direct links to the data in Massive: http://massive.ucsd.edu/ProteoSAFe/status.jsp?task=7081dfdf6eda40daaf496fea5e21e149 and https://massive.ucsd.edu/ProteoSAFe/dataset.jsp?task=533c84cd60084fcea983ab027aa6810c Direct links to the data in ProteomeXchange: https://proteomecentral.proteomexchange.org/cgi/GetDataset?ID=PXD074376 and https://proteomecentral.proteomexchange.org/cgi/GetDataset?ID=PXD074561 The uncut images of the western blots are available in the Supplementary Information Uncut gels section. Numerical source data underlying the graphs can be found in the Supplementary Data file. Other data generated in this study is available upon reasonable request from the corresponding author.

Received: 12 April 2025; Accepted: 24 February 2026;
Published online: 05 March 2026

References

1. Borisov, T., Metodiev, D., Ferdinandov, D. & Roumenina, L. T. Complement system in tumor growth and metastases. *Br. J. Cancer* https://doi.org/10.1038/s41416-025-03260-6 (2025).
2. Merle, N. S. & Roumenina, L. T. The complement system as a target in cancer immunotherapy. *Eur. J. Immunol.* **54**, e2350820 (2024).
3. Rezola Artero, M., Minery, A., Nedelcev, L., Radanova, M. & Roumenina, L. T. Complement and the hallmarks of cancer. *Semin. Immunol.* https://doi.org/10.1016/j.smim.2025.101950 (2025).
4. Roumenina, L. T., Daugan, M. V., Petitprez, F., Sautès-Fridman, C. & Fridman, W. H. Context-dependent roles of complement in cancer. *Nat. Rev. Cancer* **19**, 698–715 (2019).
5. Ajona, D., Cragg, M. S. & Pio, R. The complement system in clinical oncology: Applications, limitations and challenges. *Semin. Immunol.* **77**, 101921 (2025).
6. Ovcinnikovs, V., Dijkman, K., Zom, G. G., Beurskens, F. J. & Trouw, L. A. Enhancing complement activation by therapeutic anti-tumor antibodies: Mechanisms, strategies, and engineering approaches. *Semin. Immunol.* **77**, 101922 (2025).
7. Saxena, R., Gottlin, E. B., Campa, M. J., He, Y. W. & Patz, E. F. Complement regulators as novel targets for anti-cancer therapy: a comprehensive review. *Semin. Immunol.* **77**, 101931 (2025).
8. King, B. C. & Blom, A. M. Intracellular complement: evidence, definitions, controversies, and solutions. *Immunol. Rev.* **313**, 104–119 (2023).
9. West, E. E. & Kemper, C. Complosome — the intracellular complement system. *Nat. Rev. Nephrol.* **19**, 426–439 (2023).
10. Daugan, M. V. et al. Intracellular factor H drives tumor progression independently of the complement cascade. *Cancer Immunol. Res.* **9**, 909–925 (2021).
11. Davidson, G. et al. Mesenchymal-like tumor cells and myofibroblastic cancer-associated fibroblasts are associated with progression and immunotherapy response of clear cell renal cell carcinoma. *Cancer Res.* **83**, 2952–2969 (2023).
12. Saxena, R. et al. Promotion of an antitumor immune program by a tumor-specific, complement-activating antibody. *J. Immunol.* **212**, 1589–1601 (2024).
13. Saxena, R. et al. Complement factor H: a novel innate immune checkpoint in cancer immunotherapy. *Front. Cell Dev. Biol.* **12**, 1–9 (2024).
14. Clarke, J. M. et al. Complement factor H targeting antibody GT103 in refractory non-small cell lung cancer: a phase 1b dose escalation trial. *Nat. Commun.* **16**, 93 (2025).
15. Bond, K. H. et al. The extracellular matrix environment of clear cell renal cell carcinoma determines cancer associated fibroblast growth. *Cancers* **13**, 1–27 (2021).
16. Yap, N. Y. et al. Establishment of epithelial and fibroblast cell cultures and cell lines from primary renal cancer nephrectomies. *Cell Biol. Int.* **43**, 715–725 (2019).
17. Karlsson, M. et al. A single–cell type transcriptomics map of human tissues. *Sci. Adv.* **7**, 1–9 (2021).
18. Lin, H. et al. Mutual activation between cancer-associated fibroblasts and cancer cells facilitates growth and progression of gastric cancer. *Int. J. Clin. Exp. Pathol.* **13**, 2691–2700 (2020).
19. Liu, T. et al. Conditional knockout of telomerase reverse transcriptase in mesenchymal cells impairs mouse pulmonary fibrosis. *PLoS ONE* **10**, 1–16 (2015).
20. Kosugi, S., Hasebe, M., Tomita, M. & Yanagawa, H. Systematic identification of cell cycle-dependent yeast nucleocytoplasmic shuttling proteins by prediction of composite motifs. *Proc. Natl. Acad. Sci. USA* **106**, 10171–10176 (2009).
21. Hellwage, J. et al. Complement C3b/C3d and cell surface polyanions are recognized by overlapping binding sites on the most carboxyl-terminal domain of complement factor H. *J. Immunol.* **169**, 6935–6944 (2002).
22. Leffler, J. et al. Annexin-II, DNA, and histones serve as factor H ligands on the surface of apoptotic cells. *J. Biol. Chem.* **285**, 3766–3776 (2010).
23. Jokiranta, T. S., Hellwage, J., Koistinen, V., Zipfel, P. F. & Meri, S. Each of the three binding sites on complement factor H interacts with a distinct site on C3b. *J. Biol. Chem.* **275**, 27657–27662 (2000).
24. Smyrek, I. et al. E-cadherin, actin, microtubules and FAK dominate different spheroid formation phases and important elements of tissue integrity. *Biol. Open* **8** https://doi.org/10.1242/bio.037051 (2019).
25. Hu, J. et al. Multi-omic profiling of clear cell renal cell carcinoma identifies metabolic reprogramming associated with disease progression. *Nat. Genet.* **56**, 442–457 (2024).
26. Becht, E. et al. Estimating the population abundance of tissue-infiltrating immune and stromal cell populations using gene expression. *Genome Biol.* **17**, 1–20 (2016).
27. Merle, N. S., Church, S. E., Fremeaux-Bacchi, V. & Roumenina, L. T. Complement system part I - Molecular mechanisms of activation and regulation. *Front. Immunol.* **6**, 262 (2015).
28. Revel, M. et al. Humoral complementomics–exploration of noninvasive complement biomarkers as predictors of renal cancer progression. *Oncoimmunology* **13** https://doi.org/10.1080/2162402X.2024.2328433 (2024).
29. Roumenina, L. T. et al. Tumor cells hijack macrophage-produced complement C1q to promote tumor growth. *Cancer Immunol. Res.* **7**, 1091–1105 (2019).
30. De Vivar Chevez, A. R., Finke, J. & Bukowski, R. The role of inflammation in kidney cancer. *Adv. Exp. Med. Biol*. **816**, 197–234 (2014).
31. Kamińska, K., Czarnecka, A. M., Escudier, B., Lian, F. & Szczylik, C. Interleukin-6 as an emerging regulator of renal cell cancer. *Urol. Oncol. Semin Orig. Investig.* **33**, 476–485 (2015).
32. Chen, Q. et al. Growth-induced stress enhances epithelial-mesenchymal transition induced by IL-6 in clear cell renal cell carcinoma via the Akt/GSK-3β/β-catenin signaling pathway. *Oncogenesis* **6** https://doi.org/10.1038/oncsis.2017.74 (2017)
33. Nguyen, T. N., Nguyen-Tran, H. H., Chen, C. Y. & Hsu, T. IL6 and CCL18 mediate cross-talk between VHL-deficient kidney cells and macrophages during development of renal cell carcinoma. *Cancer Res.* **82**, 2716–2733 (2022).
34. Elvington, M., Liszewski, M. K., Bertram, P., Kulkarni, H. S. & Atkinson, J. P. A C3(H20) recycling pathway is a component of the intracellular complement system. *J. Clin. Invest.* **127**, 970–981 (2017).
35. Ault, B. H. et al. Human factor H deficiency: mutations in framework cysteine residues and block in H protein secretion and intracellular catabolism. *J. Biol. Chem.* **272**, 25168–25175 (1997).
36. Fenaille, F. et al. Site-specific N-glycan characterization of human complement factor H. *Glycobiology* **17**, 932–944 (2007).

37. Merle, D. A. et al. mTOR inhibition via rapamycin treatment partially reverts the deficit in energy metabolism caused by FH loss in RPE cells. *Antioxidants* **10**, 1–18 (2021).
38. Crosby, M. E. & Almasan, A. Opposing roles of E2Fs in cell proliferation and death. *Cancer Biol. Ther.* **3**, 1208–1211 (2004).
39. Fogal, V., Hsieh, J. K., Royer, C., Zhong, S. & Lu, X. Cell cycle-dependent nuclear retention of p53 by E2F1 requires phosphorylation of p53 at Ser315. *EMBO J.* **24**, 2768–2782 (2005).
40. Hsieh, J. K. et al. Novel function of the cyclin A binding site of E2F in regulating p53-induced apoptosis in response to DNA damage. *Mol. Cell Biol.* **22**, 78–93 (2002).
41. Gardner, W. D. & Hoch, S. O. Binding specificity of the two major DNA-binding proteins in human serum. *J. Biol. Chem.* **254**, 5238–5242 (1979).
42. Gardner, W. D., White, P. J. & Hoch, S. O. Identification of a major human serum DNA-binding protein as β1H of the alternative pathway of complement activation. *Biochem. Biophys. Res. Commun.* **94**, 61–67 (1980).
43. Edwards, M. et al. Capping protein regulators fine-tune actin assembly dynamics. *Nat. Rev. Mol. Cell Biol.* **15**, 677–689 (2014).
44. Park, S. et al. Emerging roles of TRIO and F-actin-binding protein in human diseases. *Cell Commun. Signal* **16**, 2–6 (2018).
45. Seldeen, K. L. et al. Absence of complement factor H reduces physical performance in C57BL6 mice. *Immunobiology* **225**, 152003 (2020).
46. Mahajan, S. et al. Local complement factor H protects kidney endothelial cell structure and function. *Kidney Int.* **100**, 824–836 (2021).
47. Alexander, J. J. et al. Absence of complement factor H alters bone architecture and dynamics. *Immunobiology* **223**, 761–771 (2018).
48. Meri, S. Self-nonself discrimination by the complement system. *FEBS Lett.* **590**, 2418–2434 (2016).
49. Boudhabhay, I. & Roumenina, L. T. Complement factor H: a guardian within?. *Kidney Int.* **100**, 747–749 (2021).
50. Armento, A. et al. Loss of complement factor H impairs antioxidant capacity and energy metabolism of human RPE cells. *Sci. Rep.* **10**, 1–15 (2020).
51. Li, Y. et al. Glomerular mesangial cells derived complement factor H regulates complement activation, influences cell proliferation, and maintains actin cytoskeleton. *Int. Immunopharmacol.* **154**, 114544 (2025).
52. Amornsiripanitch, N. et al. Complement factor H autoantibodies are associated with early stage NSCLC. *Clin. Cancer Res.* **16**, 3226–3231 (2010).
53. Bushey, R. T. et al. A therapeutic antibody for cancer, derived from single human B cells. *Cell Rep.* **15**, 1505–1513 (2016).
54. Bushey, R. T. et al. Antitumor immune mechanisms of the anti-complement factor H antibody GT103. *Mol. Cancer Ther.* **22**, 778–789 (2023).
55. Campa, M. J., Gottlin, E. B., Bushey, R. T. & Patz, E. F. Complement Factor H antibodies from lung cancer patients induce complement-dependent lysis of tumor cells, suggesting a novel immunotherapeutic strategy. *Cancer Immunol. Res.* **3**, 1325–1332 (2015).
56. Clarke, J. M. et al. Complement factor H targeting antibody GT103 in refractory non-small cell lung cancer: a phase 1b dose escalation trial. Nat Commun. **16**, 93 (2025)
57. Hu, J. et al. dataset from Multi-omic profiling of clear cell renal cell carcinoma identifies metabolic reprogramming associated with disease progression. *Nat. Genet.* **56**, 442–457 (2024).
58. Yu, G., Wang, L. G., Han, Y. & He, Q. Y. ClusterProfiler: An R package for comparing biological themes among gene clusters. *OMICS* **16**, 284–287 (2012).
59. Liberzon, A. et al. The molecular signatures database hallmark gene set collection. *Cell Syst.* **1**, 417–425 (2015).
60. Hu, C. et al. CellMarker 2.0: an updated database of manually curated cell markers in human/mouse and web tools based on scRNA-seq data. *Nucleic Acids Res.* **51**, D870–D876 (2023).
61. Sun, D. et al. TISCH: A comprehensive web resource enabling interactive single-cell transcriptome visualization of tumor microenvironment. *Nucleic Acids Res.* **49**, D1420–D1430 (2021).
62. Sun, D. et al. Datasets from TISCH: A comprehensive web resource enabling interactive single-cell transcriptome visualization of tumor microenvironment: UCEC_GSE139555, STAD_GSE134520, SKCM_GSE115978, PAAD_CRA001160, OV_GSE118828, NSCLC_GSE131907, NHL_GSE128531, NET_GSE140312, MCC_GSE117988, LIHC_GSE125449, KIRC_GSE111360, HNSC_GSE103322, CRC_GSE146771, CHOL_GSE125449, BRCA_GSE138536 and BCC_GSE123813. *Nucleic Acids Res.* **49**, D1420–D1430 (2021). http://tisch.comp-genomics.org/.
63. Ramos, M. et al. Multiomic integration of public oncology databases in bioconductor. *JCO Clin. Cancer Informatics.* **4**, 958–971 (2020).
64. Meylan, M. et al. Dataset from: Tertiary lymphoid structures generate and propagate anti-tumor antibody-producing plasma cells in renal cell cancer: GSE175540. *Immunity* **55**, 527–541.e525 (2022).
65. Dragon-Durey, M. A. et al. Heterozygous and homozygous factor H deficiencies associated with hemolytic uremic syndrome or membranoproliferative glomerulonephritis: report and genetic analysis of 16 cases. *J. Am. Soc. Nephrol.* **15**, 787–795 (2004).
66. Wu, J. et al. Structure of complement fragment C3b-factor H and implications for host protection by complement regulators. *Nat. Immunol.* **10**, 728–733 (2009).
67. Boldt, K., van Reeuwijk, J., Gloeckner, C. J., Ueffing, M. & Roepman, R. Tandem affinity purification of ciliopathy-associated protein complexes. *Methods Cell Biol*. **91**, 143–160 (2009).
68. Tyanova, S. et al. The Perseus computational platform for comprehensive analysis of (prote)omics data. *Nat. Methods* **13**, 731–740 (2016).
69. Szklarczyk, D. et al. The STRING database in 2023: protein-protein association networks and functional enrichment analyses for any sequenced genome of interest. *Nucleic Acids Res.* **51**, D638–D646 (2023).
70. Morgan, H. P. et al. Structural basis for engagement by complement factor H of C3b on a self surface. *Nat. Struct. Mol. Biol.* **18**, 463–471 (2011).
71. Schmidt, C. Q. et al. A new map of glycosaminoglycan and C3b binding sites on factor H. *J. Immunol.* **181**, 2610–2619 (2011).
72. Love, M. I., Huber, W. & Anders, S. Moderated estimation of fold change and dispersion for RNA-seq data with DESeq2. *Genome Biol.* **15**, 1–21 (2014).

Acknowledgements

We thank Christoph Schmidt and Jannik Sichau for providing the FH fragments employed in the SPR experiments. This work was supported by grants to LTR from: Fondation ARC pour la recherche sur le cancer (ARCPJA2023080006999), La Ligue Contre le Cancer (N/Ref: RS21/75-69), Sorbonne Université (EmergenceRecherche2024) program, Canceropole (n°2023-1-EMERG-10-INSERM IDF CENTRE EST-1) and Fondation pour la Recherche Médicale FRM team label (FRM EQU202503020008). This work is also supported by INSERM, by Sorbonne Université, by Université de Paris Cité, and by the France 2030 program through the Idex Université Paris Cité InFibrex project (ANR-18-IDEX-0001). LTR and MCD are supported by a grant for France-Brazil collaboration from CAPES/COFECUB # Me986/23 (dossier Campus France 49518WM). MRA was supported by funds of the EU MSCA project CORVOS 860044. A.Z. was supported by the Independent Research Fund Denmark, grant DFF-1025-00015B. A.A. was supported by the DFG grant AR1432/2-1. IB received PhD fellowship from Foundation pour la Recherche Médicale (FRM). NSM received a post doc fellowship by SIRIC CARPEM.

Author contributions

M.R.A., A.M., L.T.R.: conceptualization, data curation, formal analysis, supervision, validation, methodology, writing-original draft, writing-review and editing. M.R.A., A.M., M.R., A.A., M.A.J., C.S.F., C.M., M.A.D.D., J.D.D., N.M., W.H.F., M.U., L.T.R.: discussed the data and oriented research. M.R.A., A.M., M.R., A.A., M.A.J., I.B., A.Z., E.F., M.C.D., L.S., A.R., N.M.: performed research. L.T.R. secured the funding. All authors read and approved the manuscript.

Competing interests

L.T.R. declares receiving consultancy or lecturing fees from CommitBio, Erasca, Omeros, Octapharma and Alexion, and research grants from Roche, CSL Behring, CommitBio and Novartis, unrelated to this project. LTR, MR, CSF and WHF are among the co-inventors of the patent application: EP21305187.3, 2021, US20240132974A1, 2024. The other authors declare no competing interests.

Additional information

Supplementary information The online version contains supplementary material available at https://doi.org/10.1038/s42003-026-09807-4.

Correspondence and requests for materials should be addressed to Lubka T. Roumenina.

Peer review information Communications Biology thanks the anonymous reviewers for their contribution to the peer review of this work. Primary Handling Editors: Georgios Giamas and Johannes Stortz.